



On the microstructure and high-temperature stability of nano-grained Zircaloy-4

Lucia Chen^{a,b}, Zhiyang Wang^{a,*}, Hanliang Zhu^a, Patrick A. Burr^b, Jiangtao Qu^c, Yi Huang^{d,e}, Levente Balogh^f, Michael Preuss^g, Ondrej Muránský^{a,b}

^a Australian Nuclear Science and Technology Organisation (ANSTO), Lucas Heights, NSW, Australia

^b School of Mechanical and Manufacturing Engineering, UNSW Sydney, Sydney, Australia

^c Australian Centre for Microscopy and Microanalysis, The University of Sydney, Sydney, NSW 2006, Australia

^d Department of Design and Engineering, Faculty of Science and Technology, Bournemouth University, Poole, Dorset BH12 5BB, UK

^e Materials Research Group, Department of Mechanical Engineering, University of Southampton, Southampton, SO17 1BJ, UK

^f Queen's University, Mechanical and Materials Engineering, Kingston, ON, Canada

^g Monash University, Clayton, VIC, 3800, Australia

ARTICLE INFO

Article history:

Received 12 September 2021

Accepted 4 November 2021

Keywords:

Zirconium alloys

High-pressure torsion

Microstructure

Stability

ABSTRACT

A nano-grained microstructure of an α -Zr alloy (Zircaloy-4) was produced by high-pressure torsion, which shows evidence of a metastable ω -Zr phase, rather than β -Zr, determined by combining synchrotron X-ray diffraction and detailed electron microscopy observations. The ω -Zr phase is retained at ambient conditions and shows a new orientation relationship of $[\bar{1}011]_{\alpha} // [\bar{1}100]_{\omega}$ and $(\bar{1}01\bar{1})_{\alpha} // (\bar{1}\bar{1}20)_{\omega}$ with the α -Zr matrix but is thermally unstable, fully reverting back to α -Zr phase upon heating above 350 °C.

© 2021 Acta Materialia Inc. Published by Elsevier Ltd. All rights reserved.

The development of advanced fission and fusion based energy-generation systems is largely hindered by the availability of materials capable of withstanding a combination of challenging conditions of high-radiation dose, high-temperature, and corrosive environments [1–3]. Current nuclear fuel cladding and in-reactor structural components are primarily made of zirconium (Zr) alloys, due to their combination of a low neutron absorption cross-section, reasonably high strength and creep resistance, and slow corrosion kinetics in 300 °C water [4]. One strategy to improve the mechanical properties and radiation tolerance of alloys, without sacrificing their neutronic and chemical performance, is through microstructural engineering to achieve a refined microstructure down to the nanometre regime. The high density of grain boundaries (GBs) in nano-grained alloys leads to increased strength and strain hardening due to their obstruction to dislocation motion [1]. The GBs are also known to act as strong sinks for radiation-induced point defects, which results in increased tolerance to radiation damage [2,5–9].

High-pressure torsion (HPT) is a severe plastic deformation technique that refines the grain sizes of metallic materials [10]. Ap-

plied to commercially pure Zr and Zr alloys, HPT has been shown to induce grain refinement down to average grain sizes of ~ 100 nm with a stable microstructure in ambient conditions [11–16]. However, some studies also report the formation of metastable phases of Zr, including ω -Zr and β -Zr [11–13, 17–20]. When evaluating the potential applications of nano-grained materials, the thermal stability of the microstructure is paramount for the reactor operational conditions. The thermal exposure together with the large number of GBs present in nano-grained materials can destabilise the microstructure by providing a thermodynamic driving force for the grain growth and/or recrystallisation [21]. Additionally, irradiation can further enhance the destabilisation for a metastable microstructure through irradiation-enhanced grain growth [22,23].

The present study elucidates the microstructural development and the thermal stability of nano-grained HPT-processed Zircaloy-4, a common Zr alloy, using a combination of in-situ synchrotron X-ray diffraction during heating and advanced microscopy.

A hot-rolled and annealed (as-received) plate of Zircaloy-4, with a chemical composition of Zr-1.56Sn-0.22Fe-0.11Cr (wt.%), was machined into disks of 10 mm diameter and 0.8 mm thickness with the samples' normal parallel to the rolling direction (RD). HPT-processing on the machined disks was then carried out at room temperature under an applied pressure of 6.0 GPa, with 2, 5, and 10 revolutions at a rotational speed of 1 rpm. The HPT-processed samples are named hereinafter N2, N5, and N10, respectively.

* Corresponding author.

E-mail addresses: zw603@uowmail.edu.au, zhiyangw@ansto.gov.au, zhiyangwang1688@gmail.com (Z. Wang).

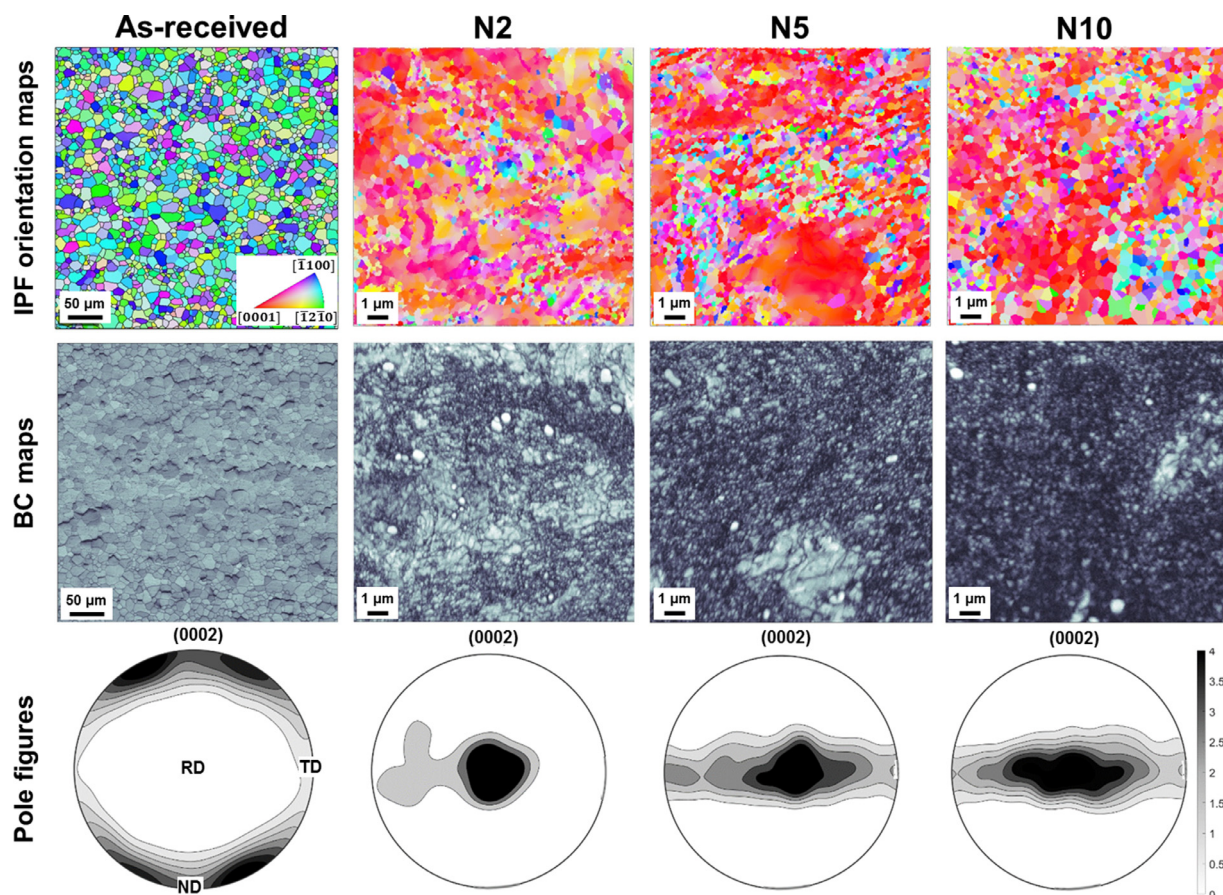


Fig. 1. EBSD-based inverse pole figure (IPF) orientation maps, band contrast (BC) maps and (0002) pole figures of the as-received and HPT-processed (N2, N5 and N10) Zircaloy-4 samples, measured from the middle-radius region of each sample. TD, ND and RD in the pole figures indicate the transverse direction, normal direction and rolling direction of the as-received plate, respectively. The centre of pole figures for the HPT disks represents the samples' normal direction which is parallel to the initial RD.

Electron Backscatter Diffraction (EBSD) observations on the as-received and HPT-processed Zircaloy-4 samples were conducted using a Zeiss® UltraPlus™ Scanning Electron Microscope (SEM) equipped with an AZtec™ EBSD system. Transmission Electron Microscopy (TEM) observations were made on the N10 sample using a JEM 2200FS TEM instrument equipped with Energy Dispersive X-ray Spectroscopy (EDS), with the TEM thin-foil sample extracted by focused ion beam (FIB) milling. A simulated selected area electron diffraction (SAED) pattern was obtained using the SingleCrystal™ program [24]. Both EBSD and TEM samples were taken from the middle-radius of the HPT disks thus avoiding regions of microstructural inhomogeneities along the disk radius [25].

Synchrotron X-ray diffraction (SXRD) measurements were performed on the 33-BM-C beamline at the Advanced Photon Source, with a monochromatic beam of energy 16 keV ($\lambda = 0.774875 \text{ \AA}$) and recorded over a 2θ range of 12° to 63° . The SXRD diffraction data were acquired from the LaB₆ standard (for the instrumental effects calibration) and HPT-processed samples at incident angles of 1° , 4° , and 10° to probe the microstructure of HPT samples further from the free surface. In-situ heating SXRD measurements were then performed on the N10 sample at the fixed incident angle of 4° in a stepwise manner from 150°C to 550°C , where the temperature was held at each step (every 50°C) for 200s for the diffraction data collection. Diffraction data was analysed using GSAS-II software [26]. Quantitative phase analysis was obtained through a full-pattern Rietveld refinements, while temperature-dependent evolution of individual peak intensities

and widths was obtained by fitting a pseudo-Voigt peak shape function.

Fig. 1 shows representative EBSD-based inverse pole figure (IPF) orientation, band contrast (BC) maps and (0002) pole figures of the as-received and HPT-processed samples (N2, N5, and N10). It becomes clear that the HPT samples have a refined, heterogeneous microstructure with a majority of nano-sized grains and few coarser micron-scale grains. Although no significant difference was observable in grain sizes amongst the N2, N5, and N10 samples, the grain size distribution appears to be the most uniform in N10. Additionally, Fig. 1 shows a consistent increase in band contrast with an increasing number of revolutions. This corresponds to an increasing fraction of dislocations, point defects, and GBs being present in the material [27]. Note that the enhanced band contrast mostly appears in the fine-grained regions while regions containing larger grains exhibit lower band contrast. Such behaviour may be related to the dynamic recrystallisation initiated by the accumulation of lattice defects coupled with a small temperature rise ($<50^\circ\text{C}$) during the HPT-processing as observed in other materials systems [28]. Together, these promote the formation of coarser, low-strain grains in the microstructure of the HPT samples.

The HPT-processing also leads to a significant crystallographic texture change - see the (0002) pole figures in Fig. 1. It is interesting to observe $\sim 90^\circ$ reorientation of the α -Zr grains. This points to profuse tensile twinning, which is activated by tension along the c-axis and reorients the α -Zr crystal lattice by 85° [29] so that the newly formed twin grains end up aligned with their c-axis along the direction of the applied pressure (i.e. initial RD). These results

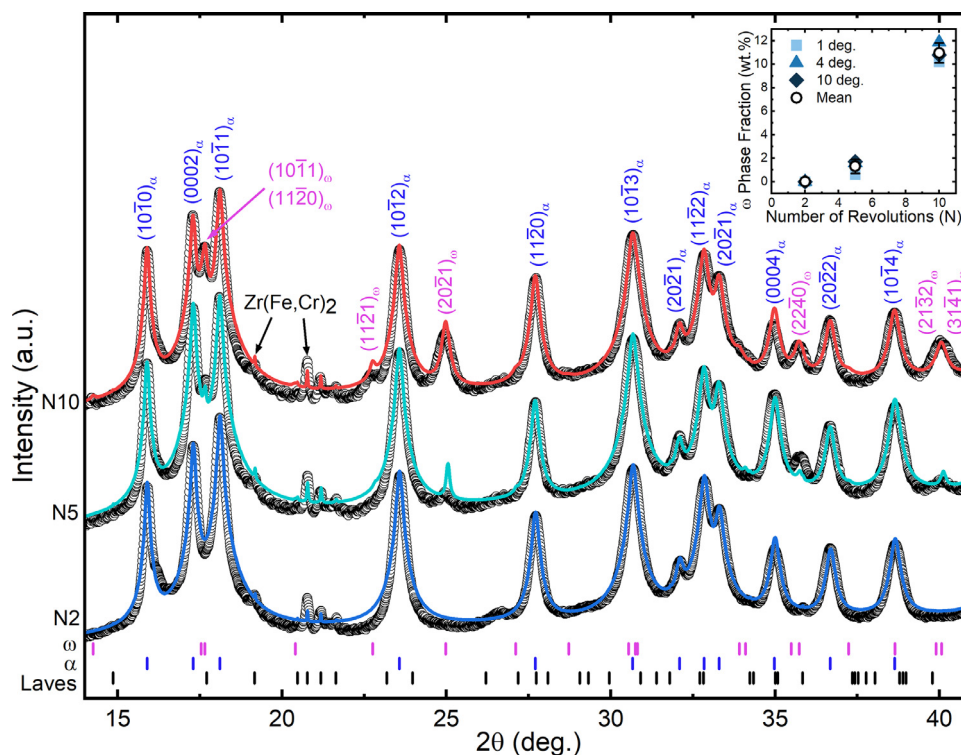


Fig. 2. SXRD patterns over a selected 2θ range of 14° to 41° collected at an incident angle of 4° , showing the development of the ω phase in the N10 sample. The graph shows the observed data points (black circles) and the Rietveld fit lines. The vertical markers show the peak positions of the corresponding phase (ω , α and Laves). Inset: ω phase fractions in the N2, N5 and N10 HPT samples, from Rietveld fittings of diffraction data measured at different incident angles (1° , 4° and 10°).

imply that the microstructure is fully reoriented by tensile twinning after only two HPT-revolutions (N2) suggesting that the twinning process contributes to the significant microstructural refinement. Additional HPT-processing (N5, N10) leads to spread of the texture along the shear direction, which are consistent with ongoing dislocation slips. This stands to reason as the tensile-twinning-reoriented microstructure is unfavourably orientated for further tensile twinning, while compression twinning is known to have considerably higher critical resolved shear stress [29]. However, we did not observe any partially twinned grains. Further studies are needed to understand the kinetics of the twin nucleation and growth during the HPT-processing.

Fig. 2 shows the Rietveld refinement result of the studied HPT samples with the high-resolution SXRD data collected at an incident angle of 4° . Note that only a section of experimental and fitted diffraction patterns is presented in Fig. 2 for clarity, however the full patterns were used for refinement. Additional diffraction peaks emerged in the N5 and N10 samples, suggesting that new phase(s) formed in these HPT samples but not in N2. One may assume that the transformation to a denser phase than α -Zr ($P6_3/mmc$, density = 6.51 g/cm^3 [30]) may be facilitated under the HPT conditions. Interestingly, it shows that the new phase was best identified as ω -Zr ($P6/mmm$, density = 6.66 g/cm^3 [31]) rather than β -Zr ($Im\bar{3}m$, density = 6.80 g/cm^3 [32]). This finding is in agreement with most previous reports of HPT-processing of pure Zr [11,13,17,18,33]. The observation can be visually seen by the indexing of the (20 $\bar{2}$ 1), (22 $\bar{4}$ 0), (21 $\bar{3}$ 2), and (31 $\bar{4}$ 1) ω peaks in the N5 and N10 data, which suggests that the critical shear strain required [16,34] for the α to ω phase transformation likely occurs between 2 and 5 revolutions under present HPT conditions.

The insert in Fig. 2 shows the phase quantification by Rietveld refinements of diffraction data at various incident angles. It reveals that only $\sim 1 \text{ wt.}\%$ ω -Zr had been formed in N5, while this value increased to $\sim 11 \text{ wt.}\%$ in N10. This observation

implies that the ω -Zr phase transformation within the material was promoted by the accumulation of the shear deformation applied above the critical shear strain required. Previous studies reported a full transformation from α -Zr to ω -Zr in pure Zr samples processed with 5-revolution HPT under similar conditions [11]. The discrepancy between this and our observations might be attributed to the α -stabilisers present in Zircaloy-4, i.e. Sn and O, retarding the ω -Zr phase transformation [35]. Interestingly, ω -Zr was not observed in [16] in which Zircaloy-4 was processed under a lower applied pressure of 3.8 GPa at 5 revolutions, indicating that the HPT-induced ω -Zr phase transformation is dependent on the applied pressure as well as the number of revolutions.

Two previous studies have reported a HPT-induced phase transformation from α to $\omega+\beta$ in pure Zr, characterised by X-ray diffraction (XRD) [36,37]. However, the XRD patterns of β and ω phases present significant overlap, leading to the conclusive characterisation of these phases being challenging. In the present work, we attempted to perform a Rietveld fit of N10 data using the $\alpha+\beta$ phase model, and the fitting yielded a quality of fit identical to that of the $\alpha+\omega$ structural model presented in Fig. 2 ($R_{wp} = 16\%$ in both cases). Although both fittings show reasonable qualities, a close inspection of the fit patterns reveals that some weak peaks in the N10 data, at 2θ of approximately 22.5° and 34.5° , were only modelled with the $\alpha+\omega$ structural model. The presence of ω -Zr, and absence of β -Zr, is further supported by the TEM analysis presented below. This result is also consistent with previous studies on the high pressure induced phase transformations in Zr showing that the high pressure tends to stabilise the ω phase rather than the β phase. Conversely, β -Zr is stabilised at high temperatures or by Nb, Fe and Cr alloying additions [17,18,38]. Zircaloy-4 contains no Nb and only minor quantities of Fe and Cr, which are almost entirely sequestered into second phase particles Laves phase $\text{Zr}(\text{Fe,Cr})_2$ [39] as detected in our high-resolution SXRD data (Fig.

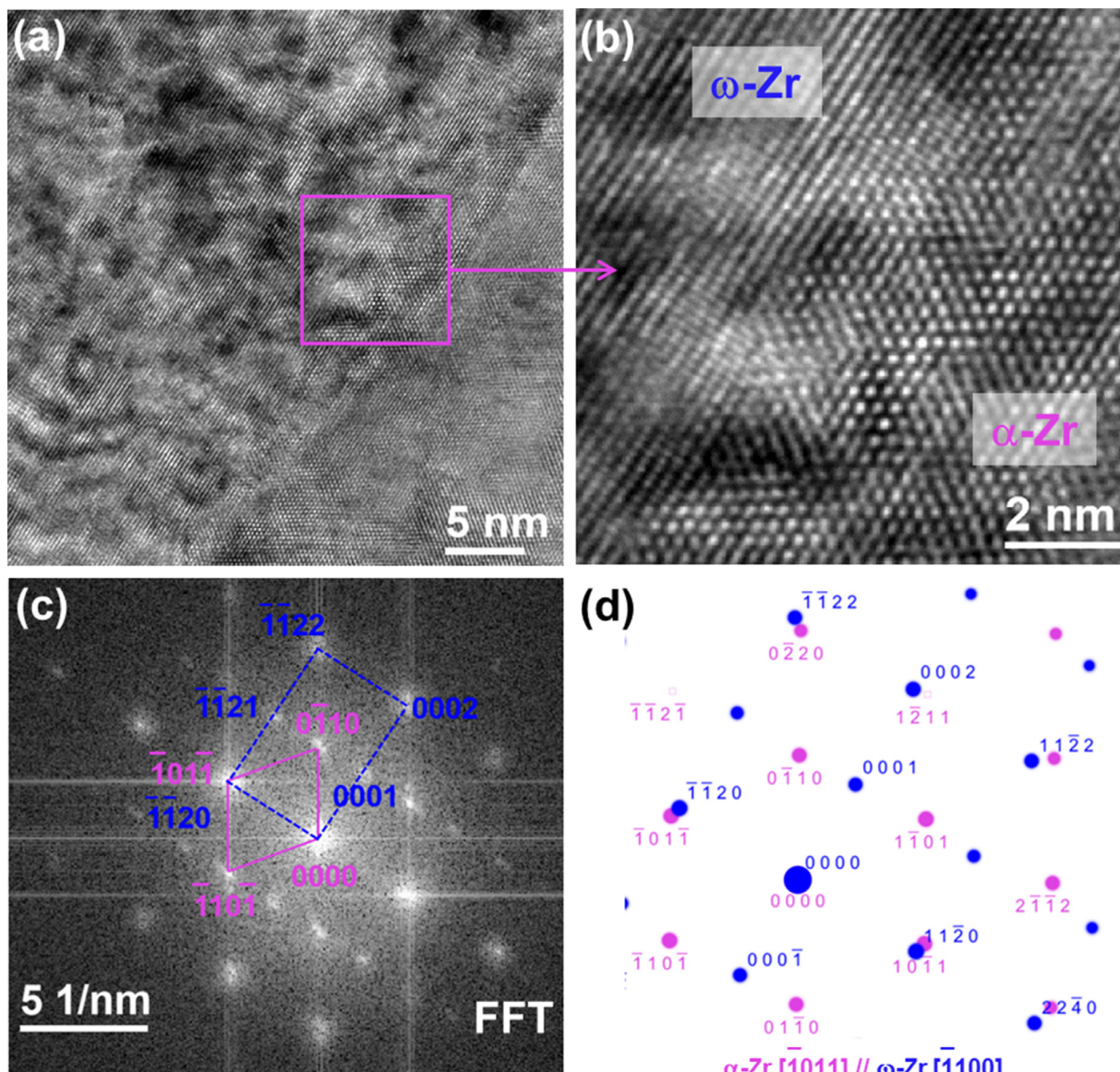


Fig. 3. Formation of the ω phase in the N10 HPT sample and its orientation relationship with the α -Zr phase. (a, b) HRTEM images. (c) the fast-Fourier transform (FFT) of Fig. b, and (d) simulated electron diffraction patterns of the ω and α phases along the $[\bar{1}011]_{\alpha}$ and $[\bar{1}100]_{\omega}$ zone axes, respectively, showing a slight misorientation of $\sim 4^{\circ}$ between the $(\bar{1}01\bar{1})_{\alpha}$ and $(\bar{1}\bar{1}20)_{\omega}$ crystallographic planes.

2). Additionally, no micro-segregation of these elements was observed in the HPT samples from the TEM-EDS experiments. Hence, it is reasonably inferred that these elements in Zircaloy-4 likely had minimal impact on the phase transformation undergone by the HPT samples.

Fig. 3 shows the TEM observation that confirms the presence of ω -Zr in the N10 sample, and no β phase was observed. Based on the fast Fourier transformation (FFT) of the high-resolution TEM (HRTEM) images in Fig. 3, an orientation relationship (OR) of $[\bar{1}011]_{\alpha} // [\bar{1}100]_{\omega}$ and $(\bar{1}01\bar{1})_{\alpha} // (\bar{1}\bar{1}20)_{\omega}$ was found between the α and ω phases. A 4° angle of misorientation was found to be present between $(10\bar{1}\bar{1})_{\alpha}$ and $(11\bar{2}0)_{\omega}$ planes. The simulated electron diffraction patterns in Fig. 3d also support this OR. Interestingly, this OR is different from those reported previously in the Zr alloy system. Under the static high pressure condition, the OR of $(0001)_{\alpha} // (11\bar{2}0)_{\omega}$, $[11\bar{2}0]_{\alpha} // [0001]_{\omega}$ were observed [40], whereas under the shock loading conditions, the $(10\bar{1}0)_{\alpha} // (10\bar{1}\bar{1})_{\omega}$, $[10\bar{1}0]_{\alpha} // [11\bar{2}\bar{3}]_{\omega}$ OR was reported [41]. The different OR compared to previous reports is likely attributed to the severe

plastic deformation process, and the accompanying formation of a large number of lattice defects.

Note that the present HRTEM image in Fig. 3a was one of two instances of ω phase identification from the many HRTEM images obtained, indicating that the residual phase fraction of ω -Zr in the TEM samples was significantly lower than that detected by SXR (D (~11 wt.% in the N10 sample)). It is considered that the low observation rate of ω -Zr from TEM is possibly related to the FIB milling for the TEM sample preparation, which may have relieved some of the elastic stresses within the grains. This process may play an important role in stabilising the ω phase.

To investigate the temperature stability of refined microstructure produced by HPT, in-situ SXR measurements during heating were performed on the N10 sample, and the results are shown in Fig. 4. While the HPT-induced ω phase was found to be metastable at ambient conditions, it is evident that it disappears entirely at a temperature of 350°C (Fig. 4a). As only the dominant α -Zr peaks remained, it can be concluded that all ω phase reverts back to the α phase when heated. Figs. 4b and c further show the evo-

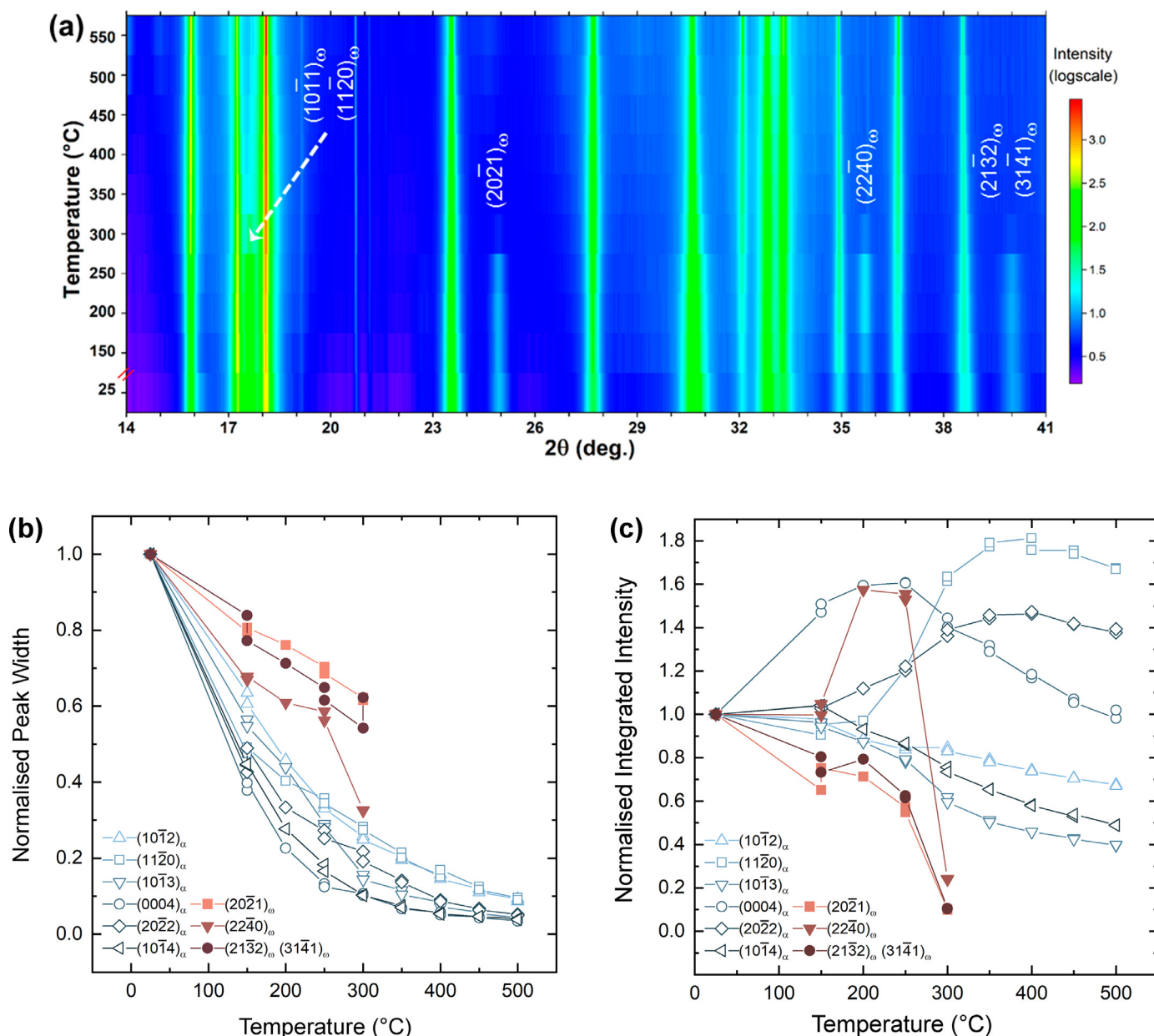


Fig. 4. High temperature SXRDX data of N10 HPT sample. (a) Contour plot of in-situ SXRDX data, and normalised (b) peak widths as well as (c) peak intensities of selected α and ω peaks as a function of temperature.

lution of normalised peak width and integrated intensity of selected α -Zr and ω -Zr diffraction peaks with increasing temperature. Fig. 4b shows that the HPT-refined microstructure was not stable at high temperatures, as indicated by the decrease in peak width observed with an increase in temperature in both the α and ω phases. This peak narrowing during heating indicates that significant grain growth of the α -Zr grains and/or annihilation of crystal defects was experienced. Using the Williamson-Hall integral breadth approach [42], the average crystallite size of the N10 sample increased from 27 to 79 nm when heated from 25 °C to 300 °C, and the micro-strain slightly decreased from 0.0027 to 0.0024.

The intensity variations for most fitted α peaks (Fig. 4c), including the increase of $(11\bar{2}0)_\alpha$ and $(20\bar{2}2)_\alpha$ peak intensities and decrease of other α peak intensities, were observed to start \sim 200 °C. These variations are associated with the α -Zr grain growth and potential recrystallisation during heating. The intensities of most fitted ω peaks were shown to decrease gradually as the temper-

ature increased. The only exception was the $(22\bar{4}0)_\omega$ peak, where an increase in normalised intensity was observed between 150 and 200 °C, possibly suggesting a change in its texture prior to transformation into α -Zr.

The results of in-situ SXRDX suggest that the heat treatment of the HPT-processed Zircaloy-4 was unable to eliminate the more brittle ω phase [43,44] whilst retaining the refined microstructure of the material. Additionally, since substantial grain growth occurred below the operating temperature of water-cooled reactors (300 °C), it appears that severe deformation processes alone may not be a viable pathway for introducing a high concentration of defect sinks in Zr alloys for practical reactor applications. The current findings emphasise that the poor thermal stability of fine-grained Zr alloys produced by severe plastic deformation needs to be addressed to achieve the enhanced radiation tolerance by the grain boundary sink effects at the reactor operational conditions. However, HPT may be a suitable method to achieve materials of

refined microstructure for fundamental studies of ion irradiation damage in Zr alloys with grain sizes down to nanoscales.

In summary, the HPT-processing of Zircaloy-4 resulted in the formation of a heterogeneous nano-grained microstructure. SXR analysis revealed the formation of approximately 1 wt.% and 11 wt.% ω -Zr after 5 and 10 HPT revolutions respectively, with the new phase retained under ambient conditions. A significantly lower occurrences of ω phase were observed from TEM compared to SXR, suggesting that some ω -Zr grains may have reverted to α -Zr during the TEM sample preparation process. Additionally, a new OR of $[1011]_{\alpha} // [1100]_{\omega}$ and $(101\bar{1})_{\alpha} // (\bar{1}\bar{1}20)_{\omega}$ was observed between ω -Zr and α -Zr. Using in-situ SXR, the ω phase was observed to fully revert back to the α phase upon heating above 350 °C, and the substantial grain coarsening of α -Zr occurs around the same temperature range. In addition, our findings caution against the identification of β phase in HPT Zr alloy samples based on XRD without complementary characterisation.

The authors acknowledge the provision of synchrotron beamtime through experimental proposal ID 60746 by the Advanced Photon Source, which was supported by the U.S. Department of Energy, Office of Basic Energy Sciences under Contract No. DE-AC02-06CH11357. The technical support of Dr. Jenia (Evguenia) Karapetrova during the beamtime experiment is acknowledged. We acknowledge travel funding provided by the International Synchrotron Access Program (ISAP) managed by the Australian Synchrotron, part of ANSTO, and funded by the Australian Government. L. Chen is supported by the Australian Institute of Nuclear Science and Engineering (AINSE). The technical assistance for TEM and EBSD sample preparation by Mr. Joel Davis and Mr. Tim Palmer (both from ANSTO) is also greatly appreciated.

Declaration of Competing Interest

The authors declare that they have no known competing financial interests or personal relationships that could have appeared to influence the work reported in this paper.

References

- [1] S.J. Zinkle, G.S. Was, *Acta Mater.* 61 (3) (2013) 735–758.
- [2] S.J. Zinkle, L.L. Snead, *Annu. Rev. Mater. Res.* 44 (1) (2014) 241–267.
- [3] T. Allen, J. Busby, M. Meyer, D. Petti, *Mater. Today* 13 (12) (2010) 14–23.
- [4] R. Krishnan, M. Asundi, *Proceedings of the Indian Academy of Sciences Section C: Engineering Sciences* 4 (1) (1981) 41–56.
- [5] M. Jin, P. Cao, S. Yip, M.P. Short, *Acta Mater.* 155 (2018) 410–417.
- [6] C. Sun, S. Zheng, C.C. Wei, Y. Wu, L. Shao, Y. Yang, K.T. Hartwig, S.A. Maloy, S.J. Zinkle, T.R. Allen, H. Wang, X. Zhang, *Sci. Rep.* 5 (2015) 7801.
- [7] P. Mao, J. Cui, Y. Chen, J. Qiu, Q. Jin, J. Qiao, Y. Zhao, K. Cui, N. Gao, K. Tai, *J. Nucl. Mater.* 526 (2019) 151741.
- [8] I.A. Ovid'ko, R.Z. Valiev, Y.T. Zhu, *Prog. Mater. Sci.* 94 (2018) 462–540.
- [9] S.J. Zinkle, 16 - Advanced irradiation-resistant materials for Generation IV nuclear reactors, in: P. Yvon (Ed.), *Structural Materials for Generation IV Nuclear Reactors*, Woodhead Publishing, 2017, pp. 569–594.
- [10] A. Zhilyaev, G. Nurislamova, B.-K. Kim, M. Baró, J. Szpunar, T. Langdon, *Acta Mater.* 51 (3) (2003) 753–765.
- [11] M.T. Pérez-Prado, A. Gimazov, O.A. Ruano, M. Kassner, A. Zhilyaev, *Scr. Mater.* 58 (3) (2008) 219–222.
- [12] A.P. Zhilyaev, A.V. Sharafutdinov, M.T. Pérez-Prado, *Adv. Eng. Mater.* 12 (8) (2010) 754–757.
- [13] R. Haraguchi, Y. Yoshimatsu, T. Nagaoka, M. Arita, K. Edalati, Z. Horita, *J. Mater. Sci.* 52 (11) (2017) 6778–6788.
- [14] S. Nikulin, S. Dobatkin, S. Rogachev, *Nanocrystalline zirconium alloys obtained by severe plastic deformation*, *J. Phys. Conf. Ser.* (2013) 012005 IOP Publishing.
- [15] K. Edalati, Z. Horita, S. Yagi, E. Matsubara, *Materials Science and Engineering: A* 523 (1) (2009) 277–281.
- [16] Y.B. Wang, M. Louie, Y. Cao, X.Z. Liao, H.J. Li, S.P. Ringer, Y.T. Zhu, *Scr. Mater.* 62 (4) (2010) 214–217.
- [17] H. Wang, W. Dmowski, Z. Wang, J. Qiang, K. Tsuchiya, Y. Yokoyama, H. Bei, T. Egami, *Appl. Phys. Lett.* 114 (6) (2019) 061903.
- [18] B. Feng, V.I. Levitas, M. Kamrani, *Materials Science and Engineering: A* 731 (2018) 623–633.
- [19] M.T. Pérez-Prado, A.P. Zhilyaev, *Phys. Rev. Lett.* 102 (17) (2009) 175504.
- [20] S.K. Sikka, Y.K. Vohra, R. Chidambaram, *Prog. Mater. Sci.* 27 (3) (1982) 245–310.
- [21] L.R. Xiao, Y. Cao, S. Li, H. Zhou, X.L. Ma, L. Mao, X.C. Sha, Q.D. Wang, Y.T. Zhu, X.D. Han, *Acta Mater.* 162 (2019) 214–225.
- [22] P. Wang, D.A. Thompson, W.W. Smeltzer, *Nucl. Instrum. Methods Phys. Res. Sect. B* 16 (2) (1986) 288–292.
- [23] Y. Zhang, M.A. Tunes, M.L. Crespillo, F. Zhang, W.L. Boldman, P.D. Rack, L. Jiang, C. Xu, G. Greaves, S.E. Donnelly, L. Wang, W.J. Weber, *Nanotechnology* 30 (29) (2019) 294004.
- [24] D.C. Palmer, *Zeitschrift für Kristallographie-Crystalline Materials* 230 (9–10) (2015) 559–572.
- [25] X.H. An, S.D. Wu, Z.F. Zhang, R.B. Figueiredo, N. Gao, T.G. Langdon, *Scr. Mater.* 63 (5) (2010) 560–563.
- [26] B.H. Toby, R.B. Von Dreele, *J. Appl. Crystallogr.* 46 (2) (2013) 544–549.
- [27] T. Maitland, S. Sitzman, *Electron Backscatter Diffraction (EBSD) Technique and Materials Characterization Examples*, Springer Berlin2007.
- [28] K. Edalati, Y. Hashiguchi, P.H.R. Pereira, Z. Horita, T.G. Langdon, *Materials Science and Engineering: A* 714 (2018) 167–171.
- [29] G.C. Kaschner, C.N. Tomé, I.J. Beyerlein, S.C. Vogel, D.W. Brown, R.J. McCabe, *Acta Mater.* 54 (11) (2006) 2887–2896.
- [30] B. Lichten, *Trans. Met. Soc. AIME* 218 (1960).
- [31] J. Jamieson, *High Temperatures-High Pressures* 5 (2) (1973) 123–131.
- [32] R. Russell, *JOM* 6 (9) (1954) 1045–1052.
- [33] A.V. Podolskiy, B.J. Bonarski, D. Setman, C. Mangler, E. Schaffler, E.D. Tabachnikova, M. Zehetbauer, *Microstructure and Properties of Nanostructured Zirconium Processed by High Pressure Torsion*, *Materials Science Forum*, *Trans Tech Publ* (2011) 433–438.
- [34] Y. Huang, M. Lemang, N.X. Zhang, P.H.R. Pereira, T.G. Langdon, *Materials Science and Engineering: A* 655 (2016) 60–69.
- [35] D.O. Northwood, D.T. Lim, *Can. Metall. Q.* 18 (4) (1979) 441–467.
- [36] M. Pérez-Prado, A. Zhilyaev, *Phys. Rev. Lett.* 102 (17) (2009) 175504.
- [37] B. Srinivasarao, A. Zhilyaev, M. Perez-Prado, *Scr. Mater.* 65 (3) (2011) 241–244.
- [38] L. Gao, X. Ding, T. Lookman, J. Sun, E. Salje, *Appl. Phys. Lett.* 109 (3) (2016) 031912.
- [39] X.Y. Meng, D.O. Northwood, *J. Nucl. Mater.* 132 (1) (1985) 80–87.
- [40] A. Rabinkin, M. Talianker, O. Botstein, *Acta Metall.* 29 (4) (1981) 691–698.
- [41] S. Song, G. Gray III, *Philos. Mag. A* 71 (2) (1995) 275–290.
- [42] H.P. Klug, L.E. Alexander, *X-ray Diffraction Procedure*, Wiley, New York, 1974, p. 505, second ed..
- [43] M.A. Kumar, N. Hilairet, R.J. McCabe, T. Yu, Y. Wang, I. Beyerlein, C.N. Tomé, *Acta Mater.* 185 (2020) 211–217.
- [44] S. Sikka, Y. Vohra, R. Chidambaram, *Prog. Mater. Sci.* 27 (3–4) (1982) 245–310.